Oscillatory relaxation of zonal flows in a multi-species stellarator plasma

E. Sánchez[1], I. Calvo[1], J. L. Velasco[1], F. Medina[1], A. Alonso[1], P. Monreal[1], R. Kleiber[2] and the TJ-II team

[1]Laboratorio Nacional de Fusión / CIEMAT. Avda Complutense 40, 28040, Madrid, Spain.
[2]Max-Planck Insitut für Plasmaphysik, Greifswald, Germany.

E-mail: edi.sanchez@ciemat.es

16 July 2018

Abstract. The low frequency oscillatory relaxation of zonal potential perturbations is studied numerically in the TJ-II stellarator (where it was experimentally detected recently for the first time [1]). It is studied in full global gyrokinetic simulations of multi-species plasmas. The oscillation frequency obtained is compared with predictions based on single-species simulations using simplified analytical relations. It is shown that the frequency of this oscillation for a multi-species plasma can be accurately obtained from single-species calculations using extrapolation formulas. The damping of the oscillation and the influence of the different inter-species collisions is studied in detail. It is concluded that taking into account multiple kinetic ions and electrons with impurity concentrations realistic for TJ-II plasmas allows to account for the values of frequency and damping rate in zonal flows relaxations observed experimentally.

Keywords: zonal flows, gyrokinetic simulations, collisional damping, multi-species, EUTERPE

1. Introduction

Sheared flows contribute to the regulation of plasma turbulence in magnetic fusion devices via the shear decorrelation effect. Turbulent structures are broken apart as a consequence of a differential rotation thus reducing the anomalous transport produced by them [2, 3]. Zonal flows (ZFs) are a particular case of sheared flows characterized by zero wavenumber in the plasma potential while they have a finite radial wavelength. Their capability of regulating transport and the mechanisms for the drift wave turbulence to produce zonal flows are now well recognized [4]. However, mechanisms other than turbulence could, in principle, originate zonal flows [1].

The question of whether ZFs can be sustained in experimental plasmas or are damped either by collisional or collisionless processes attracted some attention years ago. Gyro-fluid simulations of turbulence in plasmas predicted high transport levels derived from ITG turbulence as a consequence of the long term damping of the zonal flows implicit in the gyro-fluid models [5]. Rosenbluth and Hinton [6], using

the gyrokinetic formalism, studied for the first time the linear response of a hot (collisionless) plasma to a zonal potential perturbation in tokamaks. They treated it as an initial value problem and looked for the long term relaxation. They found that for times much longer than the typical bounce time the long-radial-wavelength macroscopic flows are not completely damped, but a residual flow survives for long times. The work was afterwards extended to study the collisional case [7] and more realistic tokamak geometries [8],[9]. Sugama and Watanabe [10, 11, 12] treated it for the case of simplified stellarator configurations finding a link between the neoclassical transport optimization and an enhancement of the residual flows in the so-called inward-shifted configurations of the LHD stellarator. Mynick and Boozer [13], using an action-angle formalism in general stellarator geometry, found a similar result.

Mishchenko et al. studied the collisionless response of a plasma to a potential perturbation in general stellarator geometry and found that a low frequency oscillation of the zonal potential appears in the relaxation [14]. This work was afterwards extended in [15] including the damping of the oscillation. The linear zonal flow relaxation was studied recently in general stellarator configurations in [16, 17] and analytical expressions for the residual level and oscillation frequency in stellarators were derived, evaluated numerically and compared to results of gyrokinetic simulations in realistic relevant configurations.

The influence of a radial electric field on the residual level of zonal flows was considered for the first time in [18], finding that a radial electric field has also a beneficial effect because, like the neoclassical optimization, it produces a reduction of the averaged magnetic drifts of trapped particles. Global gyrokinetic simulations with the code EUTERPE [19] showed a dependency of the residual level with the electric field in stellarators. The influence of the ambient electric field on the low frequency zonal flow oscillation was studied analytically and compared with simulations in [20].

The linear relaxation properties of zonal flows (residual level and oscillation frequency) in stellarators can affect the efficiency of the zonal flows in the regulation of the turbulent transport, which in turn is a non-linear problem. A positive relationship between an increased zonal flow residual and reduced turbulent transport in LHD configurations is found in [21, 22, 23], while in W7-X the residual level appears not to play an important role, but the ZF oscillation frequency seems to be related to the turbulent transport level [24]. These linear properties could provide a way to characterize stellarator configurations in respect of turbulent transport and their evaluation is relatively inexpensive [16, 17], which makes them appealing to be used in the search for stellarator optimized configurations.

While the residual zonal flow level does not appear as a quantity susceptible to direct measurement [25, 26, 27], the oscillation frequency does, and very recently an oscillatory relaxation of a (zonal) potential perturbation was experimentally detected in pellet injection experiments carried out in the TJ-II stellarator [1]. The experimental measurements were compared to global gyrokinetic simulations finding a qualitative agreement between experimental and simulated oscillation frequencies and damping rates. In that work, a single-ion plasma was considered in the simulations. In the present work the linear relaxation of zonal potential perturbations, with particular focus on the oscillation frequency and damping rate is studied in the same magnetic configuration considering collisions and extending the study to multiple-species plasmas.

The rest of the paper is organized as follows. In section 2 the code EUTERPE used for the simulations, the equations that it solves and the numerical setup are presented.

In section 3 some general properties of the zonal flow relaxation in stellarator geometry are described. In section 4 the oscillation frequency of ZFs in a multi-species plasma is studied and simulation results are compared to estimations based on single-species calculations. In section 5 the damping of the oscillations is studied in some detail and the oscillation frequencies and damping rates are calculated for the experimental conditions of our previous work [1]. Finally, section 6 is devoted to discuss the results and draw some conclusions.

2. The EUTERPE code and the numerical set-up

EUTERPE is a global gyrokinetic code aimed at simulating plasmas in three dimensional geometries [28, 29]. It solves the gyroaveraged kinetic equation

$$\frac{\partial f_a}{\partial t} + \dot{\mathbf{R}}\frac{\partial f_a}{\partial \mathbf{R}} + \dot{v_\parallel}\frac{\partial f_a}{\partial v_\parallel} = C(f_a) \tag{1}$$

for the distribution function f_a of up to three kinetic species. Here $\dot{x}{:=}\frac{\mathrm{dx}}{\mathrm{dt}}$ means time derivative.

In the electrostatic approximation here used, the equations of motion for the species a ($\dot{\mathbf{R}}$ and $\dot{v_\parallel}$) can be written as $\dot{\mathbf{R}} = \dot{\mathbf{R}}^0 + \dot{\mathbf{R}}^1$ and $\dot{v}_\parallel = \dot{v}_\parallel^0 + \dot{v}_\parallel^1$, with

$$\dot{\mathbf{R}}^0 = v_\parallel \mathbf{b} + \frac{\mu B + v_\parallel^2}{B_a^* \Omega_a}\mathbf{b}\times\nabla\mathbf{B} + \frac{v_\parallel^2}{B_a^*\Omega_a}(\nabla\times\mathbf{B})_\perp - \frac{\nabla\phi_{LW}\times\mathbf{b}}{B_a^*} \tag{2}$$

$$\dot{\mathbf{R}}^1 = -\frac{\nabla\{\phi\}_G\times\mathbf{b}}{B_a^*} \tag{3}$$

$$\dot{v_\parallel}^0 = -\mu\mathbf{b}\cdot\nabla\mathbf{B} + \frac{v_\parallel}{B_a^*\Omega_a}(\nabla\times\mathbf{B})_\perp\cdot\nabla\mathbf{B} \tag{4}$$

$$\dot{v_\parallel}^1 = -\frac{q_a}{m_a}\mathbf{b}\cdot\nabla\{\phi\}_G + \frac{q_a}{m_a}\frac{v_\parallel}{B_a^*\Omega_a}\left[\mathbf{b}\times\nabla\mathbf{B} + (\nabla\times\mathbf{B})_\perp\right]\cdot\nabla\{\phi\}_G. \tag{5}$$

The magnetic moment per unit mass, μ, is a constant of motion ($\dot{\mu} = 0$); q_a and m_a are the charge and mass respectively of the species a, $\Omega_a = q_a B/m_a$ is the cyclotron frequency, $\mathbf{b} = \mathbf{B}/B$ is the unit vector in the magnetic field ($\mathbf{B}$) direction and $B_a^* = B + \frac{m_a v_{||}}{q_a}\mathbf{b}\cdot\nabla\times\mathbf{b}$. The second and third terms in the right hand side of Eq. 2 represent the magnetic drifts. The third term is related to the pressure gradient (see [31]) and it is identically zero for a vacuum magnetic equilibrium such as the one used in this work. $\{\phi\}_G$ is the gyro-averaged potential introduced in Ref. [30]. $-\nabla\phi_{LW}$ represents the ambient, long-wavelength radial electric field, which in stellarators is, in general, determined by neoclassical processes [32]. Here it is included as a zero order contribution, i. e. it is not evolved self consistently, like ϕ in $\nabla\{\phi\}_G$ is, but it is kept fixed along the simulation. It is important to include it in the simulation because it can have an influence on the linear relaxation of zonal perturbations [20, 19]. The first term in the right hand side of Eq. 4 represents the magnetic mirror trapping and the second one is also related to the pressure gradient. Finally, the second term on the right hand side of Eq. 5 is known as the parallel nonlinearity.

In this work, the collisions between different species are taken into account using a pitch-angle scattering collision operator [33]. The contributions of inter-species collisions to $C(f_a) = \sum_b C(f_a, f_b)$ are studied separately in section 5.

The code uses a particle-in-cell scheme, the distribution function being discretized using markers whose trajectories are given by Equations 2. The δf method is used, so that the distribution function is separated into an equilibrium plus a time-dependent perturbation as $f_a(\mathbf{R}, v_{||}, \mu, t) = f_a^0(\mathbf{R}, v_{||}, \mu) + \delta f_a(\mathbf{R}, v_{||}, \mu, t)$. A local Maxwellian distribution is used as equilibrium distribution function f_a^0. Using the δf decomposition and linearizing, the kinetic equation

$$\frac{\partial \delta f_a}{\partial t} + \dot{\mathbf{R}}^0 \frac{\partial \delta f_a}{\partial \mathbf{R}} + \dot{v_\parallel}^0 \frac{\partial \delta f_a}{\partial v_\parallel} = -\dot{\mathbf{R}}^1 \frac{\partial f_a^0}{\partial \mathbf{R}} - \dot{v_\parallel}^1 \frac{\partial f_a^0}{\partial v_\parallel} + \sum_b C(f_a, f_b) \tag{6}$$

is obtained.

Two coordinate systems are used in the code: a system of magnetic coordinates (PEST-1 [34]) (s, θ^*, φ) is used for the electrostatic potential and cylindrical coordinates (r, z, φ) are used for pushing the particles, where $s = \Psi/\Psi_0$ is the normalized toroidal flux and θ^* and φ are the poloidal and toroidal angles. The equation for the electric potential is discretized using finite elements (B-splines). More details about the code can be found in the Refs [28, 29, 35, 36, 37, 38]

The simulations are initiated with a radius dependent perturbation to the ion distribution function of the form $\delta f_i \propto w(s) f_M$, where f_M is a local Maxwellian distribution and $w(s)$ is a function dependent of the radius. We use two different functions $w(s)$ in this work. For the simulations in section 3 to study the influence of the radial scale we use $w(s) = \epsilon cos(k_s s)$, with k_s defining the radial scale of the perturbation and ϵ being a small quantity (10^{-3} is used here‡) to make the initial δf part small as compared to the equilibrium distribution function. In order to emulate the experimental conditions in pellet injection experiments studied in [1] we use a different initial condition, with:

$$w(s) = \begin{cases} \epsilon & \text{in } |s - s_0| < \delta s \\ rand(\epsilon) & \text{in } |s - s_0| > \delta s \end{cases}, \tag{7}$$

where $rand(\epsilon)$ represents a random number in the interval $(-\epsilon/2, \epsilon/2)$. This function $w(s)$ represents a density perturbation radially localized around s_0. A value of 10^{-2} is used for δs.

The linearized equation (6) is solved together with the quasi neutrality equation (QNE) that, assuming a long wavelength approximation ($k_\perp \rho_i < 1$) and adiabatic electrons, reads

$$\frac{e n_{e0}(\phi - \langle\phi\rangle)}{T_e} - \nabla_\perp \cdot \left(\sum_a \frac{m_a n_{a0}}{q_a B^2} \nabla_\perp \phi \right) = \sum_a \{n_a\}_G - \sum_a n_{a0}, \tag{8}$$

where $\langle\phi\rangle$ is the potential averaged over a flux surface, $\{n_a\}_G$ is the gyro-averaged density for the ion species a and the 0 sub-index refers to the equilibrium values.

‡ As the simulations are linear and we look for the normalized potential this factor does not affect the results.

Table 1. Simulations in this work, indicating the n, T, E_r profiles, the feature studied and if impurities/collisions are used.

profiles	**set**	**feature studied**	**imp.**	**cols.**	**section**
flat n, T	A	Ω vs. k_s	-	-	3.1
exp. #39063 Fig. 3	B		-	✓	
	C	Ω, γ vs. n	-	✓	3.2
	D	Ω, γ vs. T_e, T_i	-	✓	3.3
	E	Ω, γ vs. E_r	-	✓	3.4
	F	Ω vs. Z_{eff}	Li^{3+}	-	4
	G		B^{3+}	✓	
	G	γ vs. Z_{eff}	C^{4+}		5
	H	γ vs. Z_{eff} (w/o cols. x-y)	C^{4+}	✓	5.1
exp.	I	Ω, γ experiment	C^{4+}	✓	5.2

The simulations are evolved in time and the zonal potential (m=0, n=0 Fourier component) is monitored during the simulation at several radial positions. Here m and n are the poloidal and toroidal wave numbers, respectively §. A typical time evolution of this zonal component is shown in Fig. 1.

In order to extract the values of the oscillation frequency and damping rate the potential time evolution is fit to a damped oscillation model like:

$$\frac{\phi_{00}(t)}{\phi_{00}(0)} = A\cos(\Omega t + \delta)\exp\left(-\gamma t\right) + R + \frac{c}{1+dt^e}, \tag{9}$$

where R represents the long term residual level, Ω is the oscillation frequency, γ is the damping rate and the last term represents an algebraic decay to the residual level [15]. In many practical cases, as those shown in this work, this decay is very fast and the last term in (9) can even be neglected in the fit. The fit is carried out with the non-linear fitting function *fit* from the software package Matlab.

In this work we study the linear ZF relaxation by means of numerical simulations carried out in the "standard" (100_44_64 ‖) magnetic configuration of TJ-II (magnetic field $B_T \simeq 1$ T, major radius $R = 1.5$ m, minor radius $a \simeq 0.22$ m, rotational transform $\iota = 1.55 - 1.65$). All the simulations are carried out with this vacuum magnetic equilibrium and use adiabatic electrons. In table 1 the sets of simulations presented in this work are listed, indicating if impurity and/or collisions are used and the section where they appear. We name each simulation set with labels A, B, C, ..., which are referred through the text.

3. Zonal flow relaxation in single-species stellarator plasmas

The linear relaxation of a zonal perturbation to the potential exhibits distinct features in stellarators as compared to the tokamak counterpart. In addition to the GAM oscillation observed in tokamaks [39] a new one, at a smaller frequency, appears

§ The 2D Fourier spectrum (in $\theta*$ and φ PEST coordinate angles) of the potential is calculated at each flux surface.

‖ The magnetic configurations in TJ-II are named according to the currents (in 100 A units) in the circular, helical and vertical field coils respectively, following a pattern such as ccc_hh_vv.

in stellarators, which is a completely different phenomenon related to the bounce-averaged radial drift of trapped particles [14]. We will refer to this feature as the Low Frequency Oscillation (LFO).

Depending on the magnetic configuration one of these oscillations, either the GAM or the LFO, can dominate the relaxation. The LFO has a large amplitude in W7-X while the GAM oscillation is almost imperceptible. On the contrary, in LHD (with a much smaller value of ι than W7-X) the GAM oscillation is clearly appreciable in simulations, while the LFO is almost undetectable [15, 17]. TJ-II is in between these two cases, and both oscillations are clearly appreciable in simulations, although the damping of the GAM is larger than that of the LFO [40, 17]. Here we refer to the specific case of equal ion and electron temperatures. As the frequency and damping rates of the oscillations depend also on both temperatures, the situation can be slightly different for different ratios T_e/T_i.

In this section, we study the influence of the ZF radial scale, the collisions, the temperature, and the presence of an ambient (neoclassical) electric field on the ZF relaxation process. All the simulations presented in this section include a single ion species (hydrogen) and electrons are assumed to be adiabatic.

In Fig. 1 the time evolution of the zonal potential in a linear collisionless relaxation numerical experiment in TJ-II is shown. The simulation is carried out in the standard magnetic configuration using flat density and temperature profiles with $T_i = T_e = 100$ eV and $n = 10^{19}$ m^{-3}. The simulation is initiated with a perturbation to the ion density of the form $w(s) = \epsilon cos(k_s s)$, with $k_s = 0.5\pi$. A resolution $n_s \times n_{\theta^*} \times n_\phi = 24 \times 32 \times 32$ is used in the radial, poloidal and toroidal directions, respectively, and a filter is used that retains 10 modes in both the poloidal and toroidal directions. The zonal potential time trace (normalized with its initial value) is shown in Fig. 1 for several radial positions $r/a = \sqrt{s} = 0.2, 0.4, 0.6, 0.8$. The spectra of these potential time traces, which clearly exhibit two peaks corresponding to the GAM (around 50 kHz) and LFO oscillations (around 6-9 kHz), are also shown in the same figure. As expected for a long wavelength perturbation [16] the residual level is close to zero.

3.1. Dependency on the radial scale

The relaxation of the initial perturbation shows an LFO whose frequency reasonably coincides with semi-analytical calculations [17]. In order to study the dependency of the oscillation frequency with the radial scale of the perturbation, we run a set of simulations (labeled A in table 1) using the same (flat) density and temperature profiles, with $T_i = T_e = 100$ eV and $n = 10^{19}$ m^{-3}. The simulations are collisionless, do not include $\nabla\phi_{LW}$ and are initiated with a perturbation to the ion density of the form $w(s) = \epsilon cos(k_s s)$, with different radial scales, $k_s = 0.5\pi, 1.5\pi, 2.5\pi, 3.5\pi, 4.5\pi$. The frequency is obtained from the fit of the potential time trace to the model of equation (9). As we are interested in the LFO and the early times of the time trace are dominated by the GAM oscillation we skip the first part of the time trace in the fit.

In Fig. 2, the oscillation frequency for this set of simulations is shown versus the radial position. In agreement with the theoretical expectation [17] the frequency is independent of the radial scale of the perturbation in the long wavelength limit, as shown in the figure. The dispersion in the frequency for different radial scales can be considered within the confidence level of the fitting process. Note that the

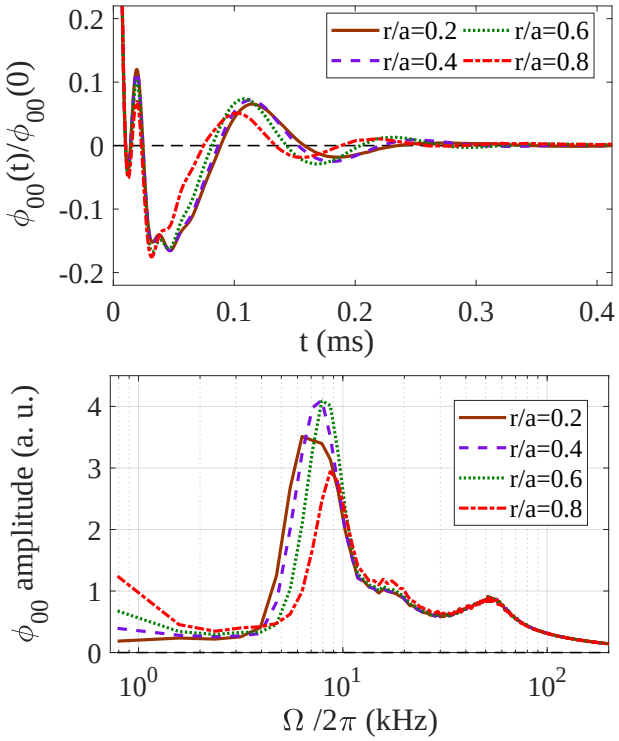

Figure 1. Time evolution of the zonal potential (normalized to its initial value) in a linear relaxation numerical experiment in TJ-II (top) and Fourier spectra of the potential time traces (bottom).

radial scale of the perturbation varies radially as the radial wave vector is $\mathbf{k_r} = k_s \nabla s$, $|\nabla s|$ having a radial dependency that approximately increases linearly with the radial coordinate r/a. There is a slight increase of the frequency with the radial position that is not related with the radial variation of k_r, but with the properties of the magnetic configuration.

Once we have shown the basic properties of ZF relaxation, and in order to approach the experimental conditions, in the following we present simulations carried out using experimental profiles from the TJ-II plasma discharge #39063, which correspond to the pellet injection experiments [41] that were analyzed in [1]. The density and temperature profiles are shown in Fig. 3. These profiles were reconstructed using an integrated procedure [42], which uses experimental data from the interferometer, the reflectometer [43], the helium beam [44], the Thomson scattering [45] and from the neutral particle analyzer (NPA) [46] diagnostics, when available. In this way the errors associated to each diagnostic and their calibration factors are taken into account for the global profile reconstruction. Only two central measurements of T_i are provided by the NPA diagnostic. The T_i radial profile is constructed with the same shape as the electron temperature one and setting the central value to the measurements provided by the NPA. The radial electric field (E_r) obtained from neoclassical calculations with DKES [47, 48] using those density and temperature experimental profiles is also shown in the same figure. No measurements

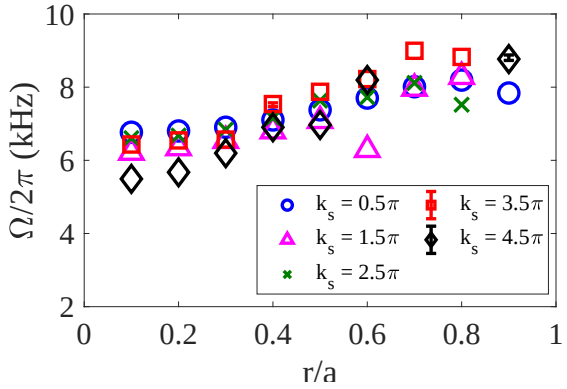

Figure 2. ZF oscillation frequency vs normalized radius in a set of simulations (A) in the TJ-II standard configuration for several radial scales of the initial perturbation, k_s.

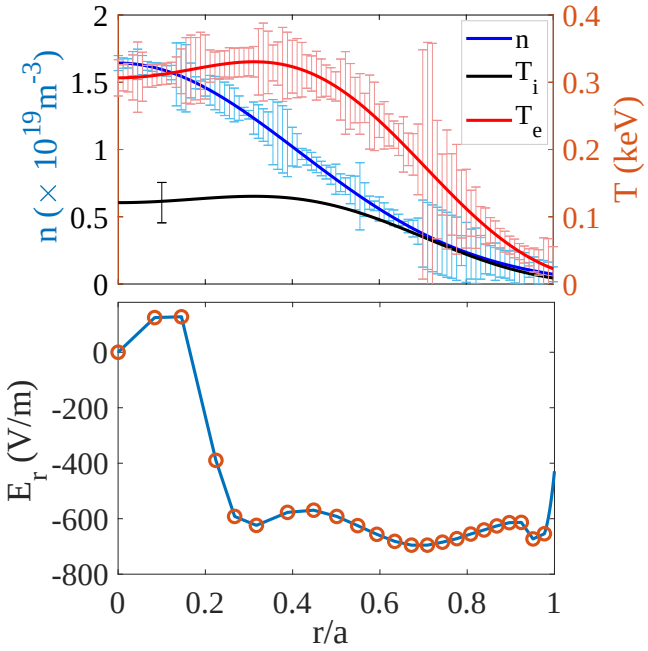

Figure 3. Density and temperature profiles in the plasma discharge #39063 of TJ-II (top) and radial electric field (E_r) obtained with DKES calculations using these n and T profiles (bottom). The error bars take into account the uncertainties in measurements of the diagnostic involved in the reconstruction (see the text)

of the electric field radial profile were available in that series of discharges.

For the sake of completeness, we show in Fig. 4 the oscillation frequency for a set of simulations (B) using the density, temperature and electric field profiles shown in Fig. 3 and with different radial scales of the perturbation, $k_s = 0.5\pi, 1.5\pi, 2.5\pi, 3.5\pi, 4.5\pi$. Its weak dependency with the radial scale is confirmed also for experimental profiles. We can see that the radial dependence of the frequency

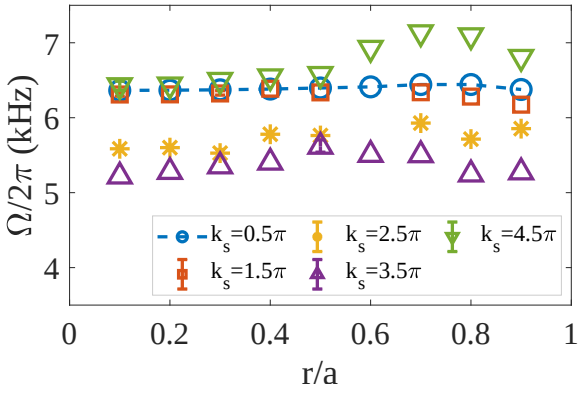

Figure 4. ZF oscillation frequency vs normalized radius in a set of simulations (B) in the TJ-II standard magnetic configuration using the density, temperature and electric field profiles shown in Fig. 3 and several radial scales of the initial perturbation, k_s.

due to the magnetic configuration properties shown in Fig. 2 is modified by the effect of the ion temperature profile. Note that this frequency does no depend on the density (see sections 3.2 and 4).

3.2. Influence of collisions

In this section, we address the influence of the collisional processes on the oscillation frequency and damping of the LFO by means of a series of single-species simulations (C) in which we change the collision frequency by changing the density while maintaining all the other parameters.

The simulations are now started with the initial condition described in (7) to emulate the situation occurring when a pellet is injected in the plasma, which suddenly increases the density at the radial location where the deposition of the particles of the pellet takes place, which is localized radially (see [49]). This initial condition in the density produces a perturbation to the plasma potential, which is obtained after the solution of the QNE in the first step of the simulation. The radial profile of this initial zonal perturbation of the potential (not shown here) is long wavelength ($\lambda_r > a$), which is important to compare with analytical predictions of the oscillation frequency in [17], which are derived under this assumption ¶. Provided that this condition is fulfilled the LFO is a robust phenomenon and its frequency does not depend on the radial scale of the perturbation, as shown previously.

We use the TJ-II standard configuration and the profiles shown in Fig. 3 with the density profile in Fig. 3 scaled by a factor. We carry out three simulations with the actual density in shot #39063, this density reduced by a factor 2 and finally with it increased by a factor 2. The results are shown in Figs. 5 and 6. Figure 5 shows the normalized potential time trace at middle radius, $r/a = 0.5$, for the three cases. It is evident from this figure that changing the density does not make a big difference in the oscillation frequency while it strongly affects the damping rate. This is even more clear in Fig. 6, which shows the frequency and damping rate extracted from

¶ Note that having this long-radial-wavelength initial perturbation to the potential is not enforced by the long-wavelength approximation used in the QNE, which is valid for $\lambda_r > \pi\rho_i$.

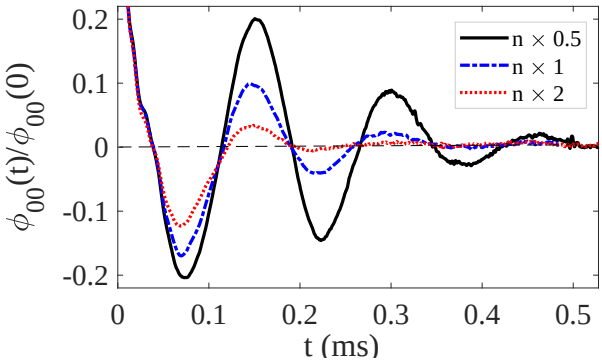

Figure 5. Normalized time trace of the potential perturbation for three simulations using the profilesin Fig. 3 with density modified by factors 0.5, 1 and 2. All cases correspond to the radial position $r/a = 0.5$.

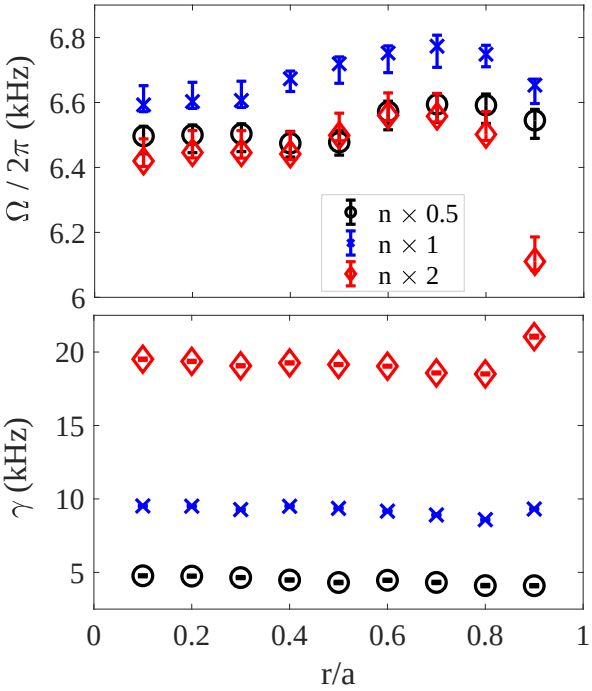

Figure 6. Frequency (top) and damping rate (bottom) for a set of simulations using the profiles shown in Fig. 3 with the density modified by several factors: 0.5, 1 and 2.

the fit to the model (9) at several radial positions for the three cases. The effect of the collisional processes on the frequency is small (less than 5%) and there is not a clear tendency with the density (collisionality), while the effect on the damping rate is almost linear with the density.

It should be taken into account that as the density is increased and the damping rate gets larger the fit is more difficult and its results become less reliable, particularly

at the outermost region of the plasma. In figs. 5 and 6 error bars corresponding to the 95% confidence level in the fit are shown. This error measure, provided by the Matlab fit routine used, is considered to be too small because it does not take into account the constrains imposed to the fitting, which also affect the result, such as the tolerance and the bound limits chosen for the parameters or the time interval at the beginning of the time trace that is skipped from the fit.

3.3. Influence of T_e and T_i

Now we address the influence of the uncertainties in the temperature profiles shown in Fig. 3 in a set of single-species simulations (D), including collisions and the experimental density and electric field profiles shown in Fig. 3. We scale the T_e or T_i profile by a factor to increase/reduce it by 25%, while keeping the other profiles. The results are shown in Fig. 7.

The influence of ion temperature on the oscillation frequency is consistent with expectations: the frequency scales with $\sqrt{T_i}$ [14, 17], and the collisional damping decreases with T_i. As expected for simulations with adiabatic electrons, T_e does not affect the oscillation frequency. Increasing T_e by 25% does not affect the damping rate, as expected, because the contribution of electrons to the collisional damping is small (see section 5). However, a reduction of the damping rate is observed when T_e is reduced by 25%. This impact of T_e on the damping is connected to the short time evolution. T_e affects the initial time evolution of the ZF relaxation, which is interpreted as a result of the strong influence of T_e on the GAM. The synergy between GAM and LFO would deserve a detailed study that exceeds the scope of this work.

3.4. Influence of the radial electric field

Although long wavelength ambient electric fields have an influence on the oscillation frequencies, which increase with its strength, for a weak enough electric field there is no dependency of the oscillation frequency on it [20]. This is the case in our conditions (Mach number $M < 10^{-2}$): including in the simulation the radial electric field shown in Fig. 3 does not change much the oscillations frequency, as shown in Fig. 8.

In this figure, we show the damping rate and oscillation frequency in a set of simulations (E) using the density and temperature profiles from Fig. 3, and including collisions. We compare simulations without the neoclassical electric field shown in Fig. 3 and also including it scaled with several factors: 0.5, 1, 1.5 and 2. It is clear from the figure that for the experimental values of E_r the influence on the oscillation frequency is small (less than 10 %), while it has a larger influence on the damping rate (around 20 %).

4. ZF oscillation frequency in a multi-species plasma

The simulations described in the previous sections included only one kinetic species (hydrogen) and electrons were assumed adiabatic. In this section, we show how the oscillation frequency in a multi-species plasma can be estimated by using calculations performed for a single-species plasma and analytic formulas. We will also calculate the oscillation frequency in multi-species plasmas, including the bulk hydrogen ion and a heavier impurity, by means of simulations.

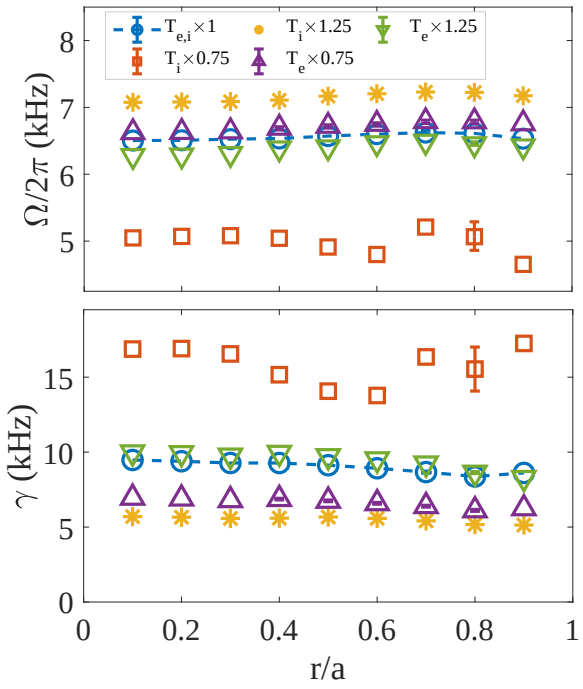

Figure 7. Frequency (top) and damping rate (bottom) for a set of simulations (D) using the profiles shown in Fig. 3 ($T_{e,i} \times 1$) and also with Te and T_i profiles from Fig. 3 scaled by factors 0.75 and 1.25.

In [17] an expression for the frequency of the LFO is derived:

$$\Omega = \sqrt{\frac{A_2}{A_1 + A_0}}, \tag{10}$$

with

$$A_0 = \sum_a \frac{n_a Z_a^2}{T_a} \left\langle |\nabla s|^2 \rho_{ta}^2 \right\rangle_r, \tag{11}$$

$$A_1 = \sum_a \frac{Z_a^2}{T_a} \{\overline{\delta_a^2} - \overline{\delta_a}^2\}_r, \tag{12}$$

$$A_2 = \sum_a \frac{Z_a^2}{T_a} \{\overline{v_{r,a}}^2\}_r, \tag{13}$$

where ρ_{ta} is the thermal Larmor radius defined as $\rho_{ta} = v_{ta}/\Omega_a$, with $v_{ta} = \sqrt{T_a/m_a}$ being the thermal velocity of species a; $\langle\rangle_r$ represents a flux surface average and the over bar means orbit average. The operation $\{\}_r$ is defined as $\{Q_a\}_r = \left\langle \int Q F_{M,a} d^3v \right\rangle_r$ and $v_{r,a} = v_{d,a} \cdot \nabla s$ is the radial magnetic drift, with

$$v_{d,a} = \frac{\mu B + v_\parallel^2}{B_a^* \Omega_a} \mathbf{b} \times \nabla \mathbf{B} + \frac{v_\parallel^2}{B_a^* \Omega_a} (\nabla \times \mathbf{B})_\perp, \tag{14}$$

and δ_a is the radial displacement from the zero-order orbit, which is obtained from the magnetic equation $v_{r,a} = \overline{v_{r,a}} + v_\parallel \hat{\mathbf{b}} \cdot \delta_a$.

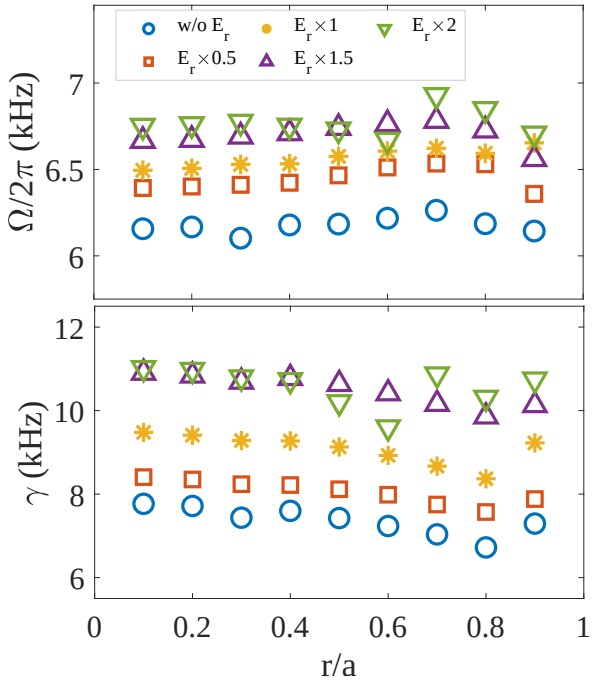

Figure 8. Frequency and damping rate for a set of simulations (E) with profiles from Fig. 3 without including the NC E_r scaled by different factors.

From expression (10), which is completely general and valid for an arbitrary number of kinetic (non collisional) species, we can see that all the kinetic species contribute to the oscillation frequency. In the expressions (11)-(13) we can separate the purely geometrical contributions from he dependency from species properties as follows:

It is easy to see that $v_{r,a}$ scales with $\frac{v_{ta}^2}{\Omega_a}$ and both ρ_{ta} and δ_a scale with $\frac{v_{ta}}{\Omega_a}$. Then, the quantities

$$\xi = \frac{\Omega_a^2 \{\overline{v_{r,a}}^2\}_r}{v_{ta}^4}, \tag{15}$$

$$\chi = \frac{\Omega_a^2 (\langle |\nabla s|^2 \rho_{ta}^2 \rangle_r + \{\overline{\delta_a^2} - \overline{\delta_a}^2\}_r)}{v_{ta}^2} \tag{16}$$

do not depend on n_a, T_a or m_a, and we can write $A_2 \sim \xi \sum_a n_a T_a$, $A_0 + A_1 \sim \chi \sum_a n_a m_a$, and the oscillation frequency as

$$\Omega = G \sqrt{\frac{\sum_a n_a T_a}{\sum_a n_a m_a}}, \tag{17}$$

with $G = \sqrt{\xi/\chi}$, related only with magnetic geometry.

We can use the expression (17) to obtain the oscillation frequency for a multi-species plasma based on the frequency for a single-species plasma as:

$$\Omega_{iz} = \sqrt{\frac{(n_i T_i + \sum_z n_z T_z) m_i}{(n_i m_i + \sum_z n_z m_z) T_i}} \Omega_i, \tag{18}$$

where the subscripts of Ω represent the species that are considered as kinetic: i for ions, e for electrons and z for an ion impurity.

As another interesting particular case, the frequency for a plasma with just an ion species and electrons, can be obtained from an adiabatic-electron calculation/simulation as:

$$\Omega_{ie} = \sqrt{\frac{(T_i + T_e)m_i}{(m_i + m_e)T_i}}\Omega_i \approx \sqrt{\frac{T_i + T_e}{T_i}}\Omega_i, \tag{19}$$

which can be computed at a much cheaper cost, as compared to the case of running a simulation with kinetic electrons.

Finally, for the case of a multi-species plasma, we can calculate the frequency, including the contribution of kinetic electrons, from the simplest calculation possible: the calculation of the frequency for a single-species with adiabatic electrons, as:

$$\Omega_{ize} \approx \sqrt{\frac{[n_i T_i + n_z T_z + (n_i + n_z Z_z)T_e]m_i}{[n_i m_i + n_z m_z]T_i}}\Omega_i, \tag{20}$$

or alternatively, from a calculation for a multi-species plasma with adiabatic electrons, as:

$$\Omega_{ize} \approx \sqrt{\frac{n_i T_i + n_z T_z + (n_i + n_z Z_z)T_e}{n_i T_i + n_z T_z}}\Omega_{iz}. \tag{21}$$

In what follows we will validate these shortcuts to obtain the oscillation frequency by comparing the estimation from simple calculations with more complete multi-species simulations, and will take advantage of these properties of the oscillation frequency to extrapolate the frequency for a multi-species plasma from single-species simulations.

We perform gyrokinetic simulations with EUTERPE in the standard magnetic configuration of TJ-II including bulk hydrogen ions and an ion impurity to validate the expression (18). We use the experimental density, temperature and the radial electric field profiles for the discharge #39063 shown in Fig. 3 and include different concentrations of the ion impurity, thus giving effective charge values in the range $1 \leq Z_{eff} \leq 2$, which are in the range of estimations for experimental discharges analyzed in [1], as we will see in 5.2. For simplicity, the density profile for the impurity ion, n_Z, is assumed equal to that of the bulk ion (hydrogen), n_0, scaled by a factor ($n_Z = f n_0$) to match the prescribed effective charge, which can be obtained right from the definition of effective charge as:

$$Z_{eff} = \frac{n_0 + n_Z Z^2}{n_0 + n_Z Z} \Rightarrow f = \frac{1 - Z_{eff}}{Z Z_{eff} - Z^2}. \tag{22}$$

We carry out simulations for three of the most common impurities in TJ-II plasmas: Li^{3+}, B^{3+} and C^{4+} both including (set G) and not including collisions (set F). The frequency is obtained with a fitting to a damped oscillation model, as explained in Section 2. The results of the extrapolation using expression (18) and a single species simulation ($Z_{eff} = 1$) are shown in Fig. 9 together with the results of the simulations. The points indicated with $\Omega_{iz}(\Omega_i)$ correspond to those obtained using the expression (18) for different values of Z_{eff}. The value Ω_i here is just that obtained in the collisionless simulation with $Z_{eff} = 1$, indicated with the dashed line.

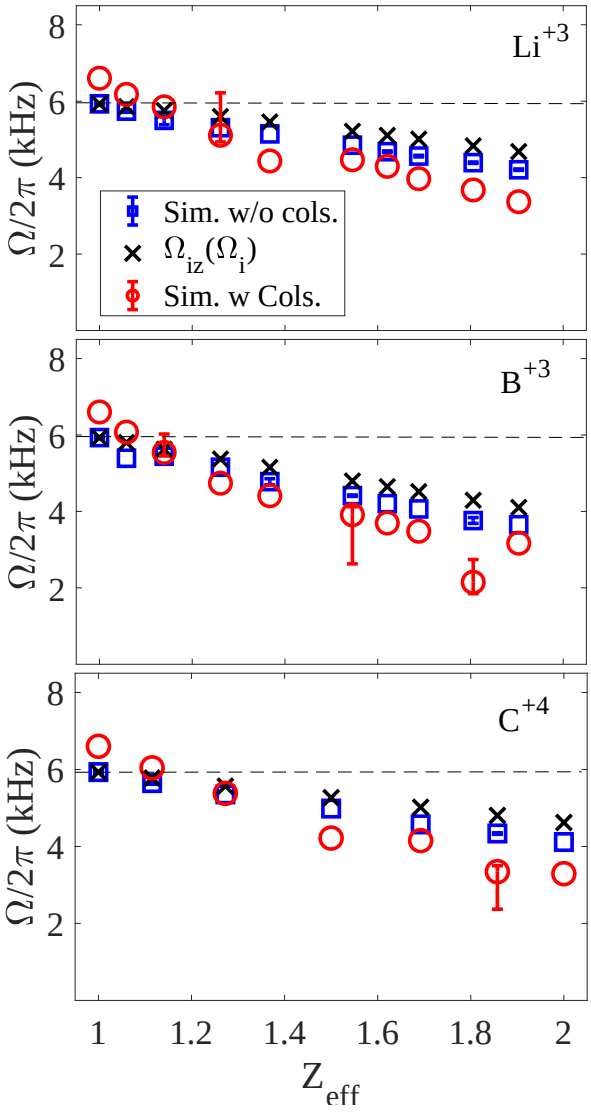

Figure 9. Oscillation frequency (Ω) vs Z_{eff} for a set of simulations with two kinetic ion species (hydrogen an a impurity) and adiabatic electrons, using the profiles shown in Fig. 3. Three different kinetic impurities are used: Li^{3+} (top), B^{3+} (center) and C^{4+} (bottom). The circles correspond to collisional simulations (G), the squares correspond to collisionless simulations (F) and the cross signs represent the results obtained from expression (18) and the collisionless $Z_{eff} = 1$ case as base for Ω_i. All the data correspond to the radial location r/a=0.5.

We can see in the figure that the agreement between the collisionless simulations and the extrapolation using expression (18) is very good for all the three impurities. In the collisional simulations, the frequency deviates slightly from the analytical prediction.

Once we have singled out the effect of the impurities, we consider now the more realistic case of a multi-species plasma with kinetic electrons, which would be the relevant one for comparison with experimental data.

Running simulations of linear ZF relaxation with kinetic electrons is much more expensive than with adiabatic electrons because the time step for the integration has to be largely reduced while a long time of simulation has to be run to cover the LFOs. This is even worse in experimentally relevant cases with electrons hotter than ions and including collisions, which requires an even smaller time integration step as compared to the collisionless case. Collisional kinetic-electron simulations run for such a long time with a short time step resulted numerically unstable in many cases even with artificially large electron mass. For this reason here we only present adiabatic-electron simulations and calculate the frequency for the kinetic-electron case using the analytic formulas (20) and (21) for extrapolation.

The estimations of this frequency for a collisionless multi-species kinetic-electron plasma using expressions (20) and (21) and collisionless simulations (F) is shown in Fig. 10 for the same three light species previously used: Li^{3+} (top), B^{3+} (middle) and C^{4+} (bottom). We plot in the same figure the frequency for a multi-species kinetic-electron plasma estimated using expression (21) and the collisional adiabatic-electron simulations (G) for Ω_{iz}. The dashed line shows the frequency for the single-species collisional adiabatic-electron case.

It is clear that taking into account the electrons increases the frequency with respect to the adiabatic electron case (as can be readily seen in expressions (19, 20) and (21), while including impurities reduces it with respect to the single-species case. Both effects compensate partially for $Z_{eff} > 1$, the degree of compensation depending on the effective charge and the collisionality. For all the impurity cases, the oscillation frequency for a multi-species plasma with kinetic-electrons estimated with expression (21) and collisional multi-species simulations is larger than that obtained by means of single-ion calculations with adiabatic electrons up to $Z_{eff} \sim 1.6$.

5. Damping of oscillations in a multi-species plasma

In this section, we study the collisional damping of ZF oscillations in a multi-species plasma. First, we calculate the damping for the collisional cases described in the previous section, including the impurities Li^{3+}, B^{3+} and C^{4+}. Next, we study in detail the different contributions from bulk ions, impurities, and electrons to the damping rate for the case of C^{4+}, which is the most likely impurity in TJ-II plasmas.

The damping rate vs the effective charge for the collisional cases (G) described in the previous section is shown for several radial locations in Fig. 11.

There is a clear increase of the collisional damping rate as the impurity concentration (Z_{eff}) increases in all cases. This result is in agreement with those presented in [50] for the damping of zonal flows in tokamaks, where impurities were found to increase the ZF damping significantly [+].

[+] Note that in [50] the reduction of the ZF residual level was studied, rather than the oscillation studied here, which is not present in an axisymmetric device [17]

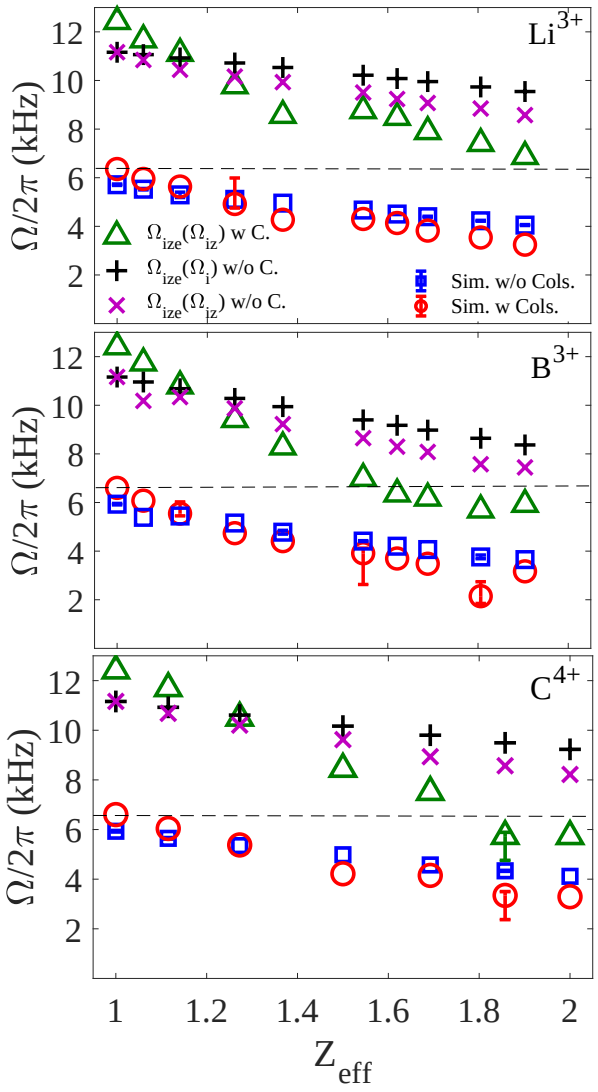

Figure 10. Ω vs Z_{eff} in a multi-species kinetic-electron plasma with the profiles shown in Fig. 3, including a kinetic impurity: Li^{3+} (top), B^{3+} (center) and C^{4+} (bottom). The two different extrapolations to the kinetic-electron case, using expressions (20 and (21), and collisionless calculations of Ω_i and Ω_{iz}, are shown with "+" and "×" signs, respectively. The circles correspond to collisional multi-species simulations (G) and the squares to the collisionless (F) cases (the same data shown in Fig. 9). The triangles correspond to the frequency for a kinetic-electron plasma extrapolated using the expression(21) and collisional simulations. All the data correspond to r/a=0.5.

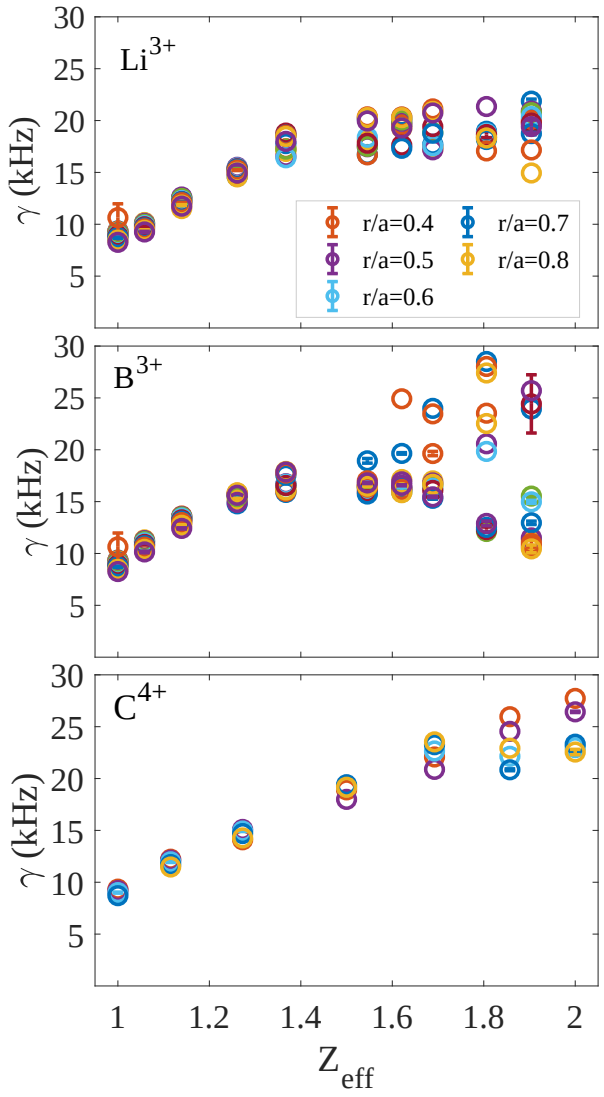

Figure 11. Damping rate (γ) vs Z_{eff} in a set of multi-species simulations (G) using the profiles shown in Fig. 3 and including a kinetic impurity: Li^{3+} (top), B^{3+} (center) and C^{4+} (bottom).

The results for the three impurities studied are very similar. For the highest values of Z_{eff} in Fig. 11 the damping increases notably and the fit of the oscillations to the model (9) is less reliable. This is the reason for the dispersion found in the damping rate, particularly in the case of B, for values of effective charge $Z_{eff} > 1.7$. The error bars provided by the fitting routine (when available) are smaller than the dispersion of results, which is considered due to the fact that the fit routine does not take into account all the parameters that affect the fit. As we will see in section 5.2 the estimated Z_{eff} for experimental discharges in [1] are below 1.8.

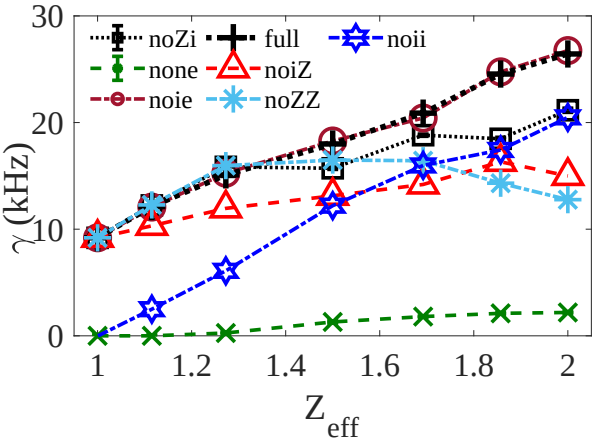

Figure 12. Damping rate (γ) vs Z_{eff} for a set of simulations (H) with the profiles shown in Fig. 3 and including H^+ (bulk) and C^{4+} kinetic ions and all collisions between bulk ions, electrons and impurity ions ("full"), without any collisions ("none"), excluding $H-H$ collisions ("noii"), excluding $H-C$ collisions ("noiZ"), excluding $C-H$ collisions ("noZi"), excluding $H-e$ collisions ("noie") and excluding $C-C$ collisions ("noZZ").

5.1. Contribution of inter-species collisions to the damping

In this section, we study the different contributions to the collisional damping of ZF oscillations separately. We will carry out the study only for the most likely impurity under the conditions of plasmas analyzed in [1], C^{4+}. The results shown in the previous section were very similar for the three impurities studied and then similar results in the individual contributions of inter-species collisions can be also expected for different impurities. The main differences between cases with different impurities in Fig. 11 was for effective charge $Z_{eff} > 1.8$, which are above the experimental values and have a strong damping. We use the same density, temperature, and electric field profiles corresponding to the discharge #39063 (shown in Fig. 3), as in previous sections. The damping rate, γ, is shown versus effective charge, Z_{eff}, in Fig. 12 for several cases in which different inter-species collisions are suppressed. First, it is shown the collisionless case (indicated as "none" in figure) and the full collisional case ("full" in the figure). We show in the same figure five more cases: excluding bulk ion (H-H) collisions ("noii"), excluding C-C collisions ("noZZ"), excluding the collisions between the bulk ion and C ("noiZ"), excluding collisions between C and the bulk ions ("noZi") and finally excluding collisions between the bulk ion and electrons ("noie"). In all cases, the same pitch-angle scattering collision operator is used [33]. The results are shown in Fig. 12 for the specific radial position $r/a = 0.5$. There is not an important dependency with radial position, as could be expected from Fig. 11 in which the full damping rates for several radial positions were shown together. This set of simulations is labeled as H in table 1.

It is clear from the figure that the collisional damping is much larger than the collisionless one, by more than a factor 10. The collisional damping is dominated by collisions between bulk ions while those of bulk ions with electrons are almost not relevant, as expected. The next contribution is that coming from collisions between bulk ions and C for $Z_{eff} < 1.7$, while the importance of the contribution from $C-C$

Table 2. Effective charge estimated from experimental SXR measurements in plasma discharges studied in [1]

shot	39047	39048	39050	39056	39058	39063	39064
Z_{eff}	1.29	1.36	1.30	1.72	1.78	1.28	1.29

collisions increases for $Z_{eff} > 1.5$. The contribution of impurities colliding with bulk ions is always very small.

5.2. Oscillatory relaxation under experiment-relevant conditions

Finally, in this section, we calculate the oscillation frequency and damping rate for multi-species plasmas, including bulk hydrogen ions, a light impurity, and adiabatic electrons, under experimentally relevant conditions. We study the pellet injection experiments analyzed in [1], and present simulations for the discharges that showed clear oscillatory relaxations, which are listed in table 2. In this case, we use the values of effective charge estimated for these discharges from experimental soft X-ray (SXR) measurements. To this end information about the plasma composition is required, which is obtained from four detectors equipped with four different Be filters [51] that respond differently with the plasma composition. Filter thicknesses were chosen to discern the presence of some of the main impurities in TJ-II plasmas (Li, B, C, O and in much less quantity F). The IONEQ code [52] is used to estimate the SXR emissivities. In this way, Z_{eff} is obtained from the absolute and relative values of the experimental signals, as well as a rough estimation of plasma composition.

The dominant impurity ion in these plasmas was estimated to be C^{4+}. The estimated values of Z_{eff} for the experimental discharges reported in [1] as showing an oscillatory relaxation, always in the range $1 < Z_{eff} < 1.75$, are shown in table 2. These values are central Z_{eff} estimations, which can be considered an upper limit for the effective charge, because the impurity concentration is maximum at the center.

In the simulations, the experimental density and temperature profiles and neoclassical electric field obtained from them corresponding to the set of plasma discharges studied in [1], #39047-39064, are used. The profiles for the discharge #39063 are shown in Fig. 3. For simplicity, the density profile for the impurity ion is assumed equal to that of the bulk ion (hydrogen) scaled by a factor to match the prescribed (experimental) effective charge in all radii. The required factor is obtained using the expression (22). We run a set of simulations (I) including collisions, C^{4+} as impurity and use adiabatic electrons. In figure 13 we show (in blue) the values of damping rate vs oscillation frequency obtained from the fit of the potential time traces for these simulations. The oscillation frequency is obtained from these multi-ion simulations and extrapolated to the kinetic-electron case using the formula (21). The damping rates are those directly obtained in the adiabatic-electron multi-species simulations. The error bars represent the uncertainty in the estimation of the frequency and damping rate through the fit to the model.

In the same figure the results obtained from simulations with single hydrogen ion species and adiabatic electrons (shown in gray color), which were presented in [1], are included for comparison. Several points corresponding to the values at several radial positions in the range of radial locations of measurements reported in [1] ($0.35 < r/a < 0.8$) are plotted in the figure, both for the single-species and the multi-species cases.

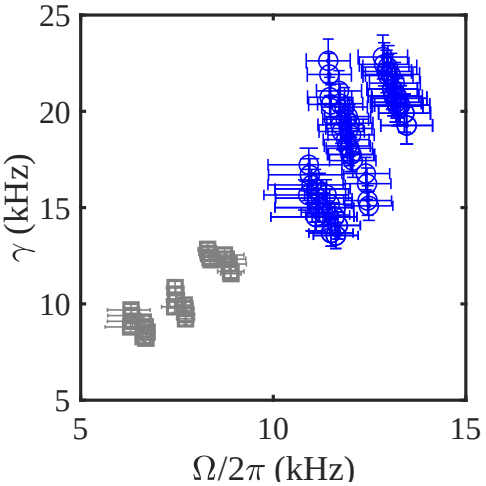

Figure 13. Damping rate (γ) vs frequency (Ω) obtained in a set of simulations (I) using n, T and E_r (NC) experimental profiles for the set of experimental discharges in table 2, and including C^{4+} kinetic impurity. Results for the multi-species kinetic-electron case (blue) and from single-species simulations with adiabatic electrons (gray) are shown (see text for details). The data correspond to $0.35 < r/a < 0.8$.

The results in the single-species case, although in qualitative agreement with the experimental measurements have both damping rates and oscillation frequencies smaller than those estimated from experimental measurements (see [1]).

It is clear from the figure that including an ion impurity in the simulation with realistic impurity concentration values and taking into account the contribution of electrons introduces a larger dispersion of results and increases significantly both the damping rate and the frequency. From this, we can conclude that the presence of impurities, even at small concentration is an important factor to be taken into account for quantitative comparison with experiments.

6. Discussion and conclusions

The linear relaxation of a zonal potential perturbation has been studied in the standard configuration of TJ-II as an initial value problem by means of global gyrokinetic simulations with the code EUTERPE. We focus our study on the low frequency oscillation characteristic of stellarators [14] rather than the GAM oscillation [39] usually observed in tokamaks. It has been shown that, in the long-wavelength limit, the oscillation frequency is not dependent on the radial scale of the potential perturbation, as expected from theory.

We have analyzed the oscillation close to the experimental conditions of the plasmas in which the LFO was detected in TJ-II [1], using experimental density and temperature profiles and the background radial electric field obtained from neoclassical calculations with DKES. It has been shown that including this radial electric field does not modify much the oscillation frequency with respect to the value without electric field, while it has a larger effect on the damping rate.

The influence of the collisionality has been addressed in simulations using a

pitch-angle collision operator. In a set of simulations with a single ion species and adiabatic electrons, the oscillation frequency has been shown to be almost unaffected by collisional processes in this range of collisionality, while the damping rate of the oscillations is largely affected, increasing approximately linearly with the density.

The oscillatory relaxation of ZFs in a multi-species plasma has been studied in experimental plasma conditions by means of simulations with two ion species and adiabatic electrons. The frequency has been shown to be reduced when an impurity ion is included at moderate (experimental) concentrations. The oscillation frequency obtained in multi-species simulations in a wide range on impurity concentration has been compared to the values predicted by means of analytical formulas and based on single-species calculations finding a very good agreement.

It has been shown that the presence of a heavier ion species increases the damping with respect to the case with single-ion species. The contribution of the different inter-species collisions to the damping of the oscillations has been studied in a set of simulations including C^{4+} impurity with specific inter-species collisions deactivated. The collisional damping is found to be much larger than the collisionless one. It was found that the most important contribution to the damping comes from collisions between bulk ions while those between ions with electrons is almost not relevant. The collisions of bulk ions with C impurity ions are important for small values of the effective charge while the contribution of C-C ions increases for effective charge above 1.7.

The oscillation frequency and damping rate has been studied in experimental plasma conditions in which the LFO was detected in TJ-II (see [1]) in simulations with adiabatic electrons and including the dominant impurity ion in these TJ-II plasmas, C^{4+}, with concentrations in the range of estimations of Z_{eff} from SXR experimental measurements for those plasma discharges. The resulting oscillation frequencies and damping rates are much closer to the experimental measurements presented in [1] than previous estimations based on single-species simulations used in that reference.

Two important conclusions can be extracted from this work. The first conclusion is that the ZF oscillation frequencies and damping rates obtained in simulations including multi-species plasmas with realistic concentration of impurities is in quantitative agreement with the experimental measurements in TJ-II [1]. It has to be taken into account that these results were obtained in multi-species simulations with adiabatic electrons. A small contribution to the damping rate can be expected from kinetic electrons. However, the contribution of electrons to the oscillation frequency could be reduced if they are in a very collisional regime.

A second important, and more general, conclusion that can be drawn is that the ZF oscillation frequency in a multi-species low-collisionality plasma can be accurately estimated from single-species calculation/simulations, which can be carried out at a much smaller computational cost.

In ref. [17] analytical formulas were derived for the oscillation frequency in general stellarator geometry that can be evaluated at a cheaper cost than gyrokinetic simulations. However, in this work we have used simulations rather than semi-analytical calculations, for all the calculations. The reason is that the expressions derived in [17] do not take into account the radial electric field, nor the gradients in the density and temperature profiles and collisional processes, which all play a role in the quantitative comparison with experimental measurements. It should be noted that the analytical expressions still have interest because they can capture the influence of the magnetic configuration at a cheaper computational cost than the gyrokinetic

simulations. In addition, we have shown in this work that the oscillation frequency is not much modified by the background electric field nor the collisional processes under the experimental conditions described in [1], however, this can not be assumed true in general.

As can be clearly seen in expression (10) derived in [17] the ZF oscillation frequency involves quantities that are averaged over the full flux surface. This indicates that the minimum computational domain to study this problem in a stellarator is a full-flux-surface, yet radially-local, physical domain. Comparison of ZF relaxation in different computational domains are in progress and have already evidenced important discrepancies between flux tube (radially local) and radially global calculations [53]. Thinking of non-linear turbulence simulations in which the zonal flow response can be relevant for the turbulence saturation the computational domain used in the simulation can also make an important difference.

This low frequency ZF oscillation may be important in W7-X configurations, because according to calculations it has a large amplitude and small collisionless damping rate [17] and could affect the turbulent transport level [54]. As W7-X operates in a less collisional regime than TJ-II, the damping will be much smaller in that case, and then the oscillation should be easier to detect than in TJ-II. Estimations of effective charge in OP1.1 experimental campaign give $1.5 < Z_{eff} < 5.5$. Then, in order to make a quantitative comparison between calculations/simulations and experimental measurements the corrections due to the presence of multiple ion species and kinetic electrons here studied will be required.

7. Acknowledgements

This work has been partially funded by the Ministerio de Economía y Competitividad of Spain under project ENE2015-70142-P. The authors thankfully acknowledge the computer resources, technical expertise and assistance provided by the Barcelona Supercomputing Center-Centro Nacional de Supercomputación and the CIEMAT computing center.

This work has been carried out within the framework of the EUROfusion Consortium and has received funding from the Euratom research and training programme 2014-2018 under grant agreement No 633053. The views and opinions expressed herein do not necessarily reflect those of the European Commission.

References

[1] Alonso J A et al. 2017 *Phys. Rev. Lett.* **118** 185002
[2] Biglari H, Diamond P H, and Terry P W 1990. *Phys. Fluids B* **2**
[3] Hahm T S 1997. *Phys. lasmas* **4 (11)** 4074
[4] P H Diamond et al. 2005 *Plasma Phys. Control. Fusion* **47** R161
[5] Glanz J. 1996 *Science* **274** 5–7
[6] Rosenbluth M N and Hinton F L. 1998 *Phys. Rev. Lett.* f80 724–727
[7] Hinton F L and Rosenbluth M N 1999 *Plasma Phys. Control. Fusion* **41** 653–662
[8] Xiao Y and Catto P J. *Phys. Plasmas* 13 1–11
[9] Xiao Y, Catto P J and Dorland W 2007 *Phys. Plasmas* 14 55910-55916
[10] Sugama H and Watanabe T H 2005 *Phys. Rev. Lett.* 94
[11] Sugama H and Watanabe T H 2006 *Phys. Plasmas* 13
[12] Watanabe T H, Sugama H, and Ferrando-Margalet S 2008 *Phys. Rev. Lett.* 100 195002–195004
[13] Mynick H E and Boozer A H 2007 *Phys. Plasmas* 14 72507–72508
[14] Mishchenko A, Helander P, and Könies A. 2008 *Phys. Plasmas* 15 72309
[15] Helander P et al. *Plasma Phys. Control. Fusion* 53 54006

[16] Monreal P et al. 2016 *Plasma Phys. Control. Fusion* 58 2–5
[17] Monreal P et al. 2017 *Plasma Phys. Control. Fusion* 59 065005
[18] Sugama H andWatanabe T H 2009 *Phys. Plasmas* 16 1–10
[19] Kleiber R, Hatzky R, and Mishchenko A 2010 *Contrib. Plasma Physics* 50
[20] Mishchenko A and Kleiber R 2012 *Phys. Plasmas* 19 072316
[21] Watanabe T H, Sugama H, and Ferrando-Margalet S 2008 *Phys. Rev. Lett.* 100 195002
[22] Nunami M et al. *Phys. Plasmas* 19 042504
[23] Nunami M, Watanabe T H, and Sugama H 2013 *Phys. Plasmas* 20 092307
[24] Xanthopoulos P et al. *Phys. Rev. Lett.* 107 245002
[25] Velasco J L et al. *Phys. Rev. Lett.* 109135003
[26] Alonso J A et al. 2013 *Plasma Phys. Control. Fusion* 55 014001
[27] Velasco J Let al. 2013 *Plasma Phys. Control. Fusion* 55 124044
[28] Jost Get al. 2011 *Phys. Plasmas* 8 3321
[29] Kornilov V et al. 2004 *Phys. Plasmas* 11 3196–3202
[30] Hahm T S 1988. *Phys. Fluids* **31** 2673
[31] D'haeseleer W D, Hitchon W N G, Callen J D, Shohet J L. 1991. *Flux coordinates and magnetic field structure: a guide to a fundamental tool of plasma theory* (Berlin: Springer-Verlag)
[32] Helander P and Simakov A N 2008 *Phys. Rev. Lett.* 101 145003
[33] Kauffmann K et al. 2010 *Journal of Physics: Conference Series* 260 012014
[34] Grimm R C, Greene J M, Johnson J L. 1976 *Methods in Comp. Phys.* 16 253
[35] Kornilov V, Kleiber R, and Hatzky R. 2005 *Nuclear Fusion* 45 238
[36] Kleiber R et al. 2006 *Theory of Fusion Plasmas.* 871 AIP Conference proceedings 1. AIP, 2006, pp. 136–146.
[37] Kleiber R and Hatzky R. *Comput. Phys. Commun.* 183 305–308
[38] Borchardt M, Kleiber R , and Hackbusch W *Journal of Computational Physics* 231 6207–6212
[39] Winsor N , Johnson J L , Dawson J M 1968 *Phys. Fluids* 11 2448
[40] Sánchez E et al. *Plasma Phys. Control. Fusion* 55 014015
[41] McCarthy K J et al. 2017 *Nuclear Fusion* 57
[42] van Milligen B Ph et al. 2011 *Rev. Sci. Instr.* 82 073503
[43] Estrada T et al. *Plasma Phys. Control. Fusion* 43 1535–1545
[44] B Brañas et al. 2001 *Rev. Sci. Instr.* 72 602–606
[45] Herranz Jet al. 2003 *Fusion Engineering and Design* 6 525–536
[46] Fontdecaba J.M. et al. 2004 *Fusion Sci. Tech.* 46
[47] Hirshman S al. 1986 *Phys. Fluids* 29
[48] Velasco J L and Castejón F 2012 *Plasma Phys. Control. Fusion* 54 15005
[49] Velasco J L et al. 2016 *Plasma Phys. Control. Fusion* 58 084004
[50] Braun S et al. 2009 *Plasma Phys. Control. Fusion* 51
[51] Baião D et al. 2010 *Rev. Sci. Instr.* 81 10–711
[52] Weller A, Pasini D, and Edwards AW 1987 *Joint Europ. torus*
[53] J Smoniewski et al. 59th Annual Meeting of the APS Division of Plasma Physics, 2017. To be published.
[54] Xanthopoulos P et al. *Phys. Rev. Lett.* 107 245002